Longitudinal thermalization via the chromo-Weibel instability

Maximilian Attems
Frankfurt Institute of Advanced Studies

arXiv:1207.5795

Collaborators: Anton Rebhan, Michael Strickland

November 22, 2012

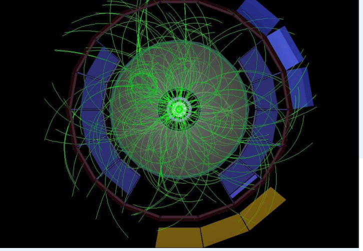

Motivation

SU(N) Yang-Mills field dynamics

Weakly coupled inspired by Hard Thermal Loops (HTL)

Real-time physical quantities of non-equilibrium processes

Plasma turbulence affects parton transport (isotropization, jet energy loss, viscosity,..)

Early time dynamics of the quark gluon plasma

Derivation of time scales for the isotropization, thermalization

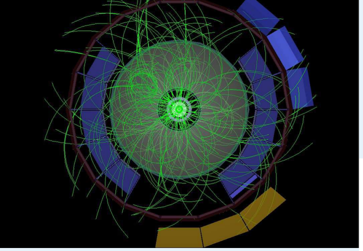

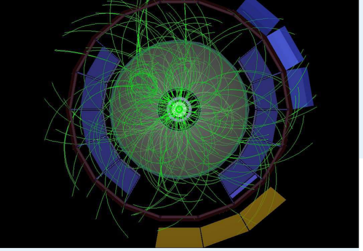

Hard-Expanding Loops Assumptions

Free streaming background

Anisotropy in momentum space

SU(2) particle content

Fixed transverse size

Extrapolate to $\alpha_s \sim 0.3$

Match CGC $n(\tau_0) \propto Q_s^3 \alpha_s^{-1}$

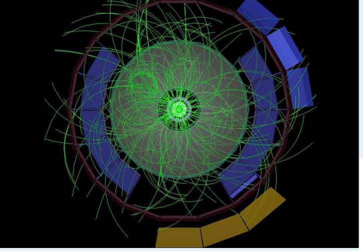

Stages of the Little Big Bang

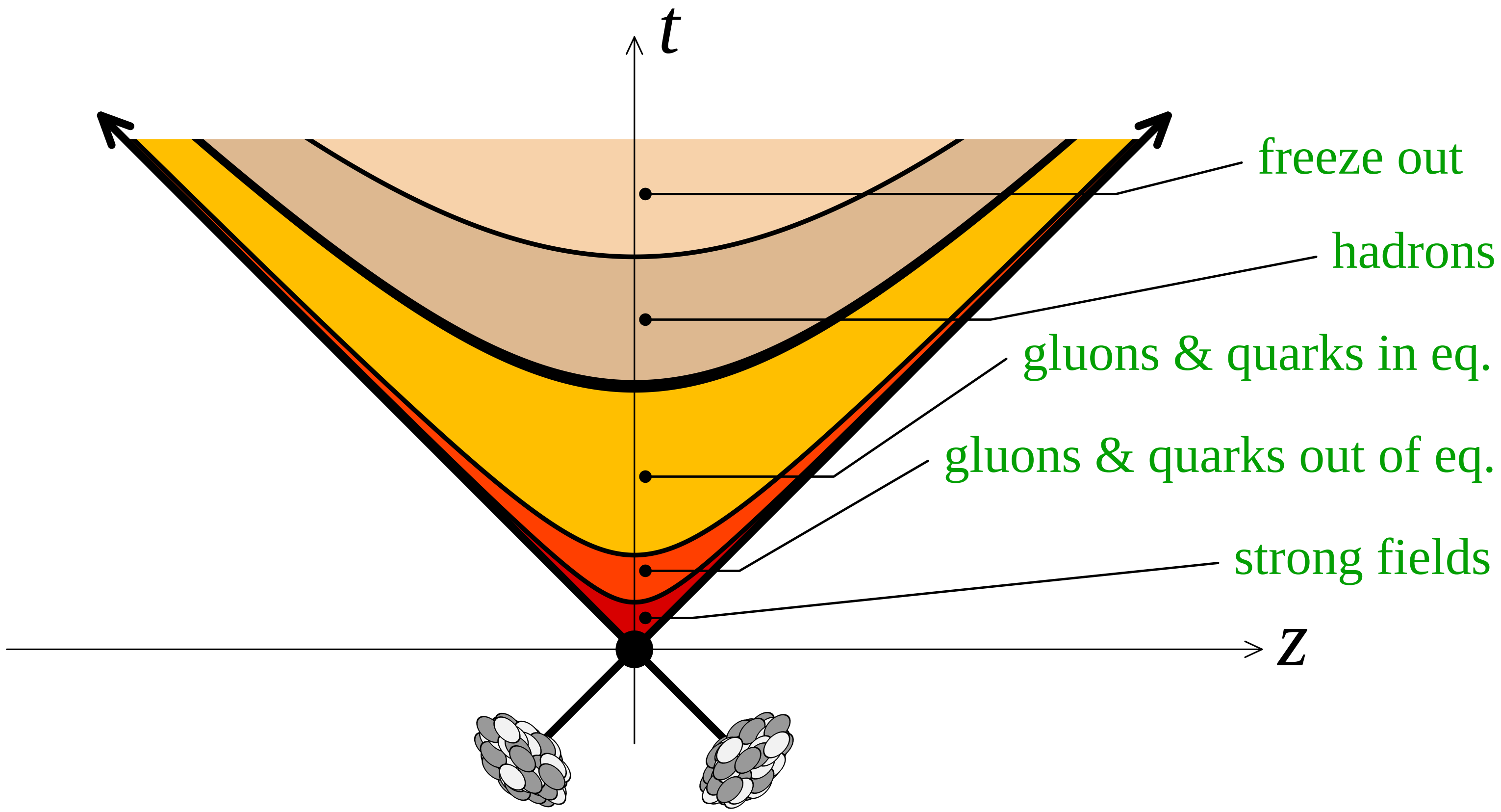

[Gelis 2010] Illustration of the stages of a heavy ion collision. This work focuses on the early phase with strong fields in an out of equilibrium situation.

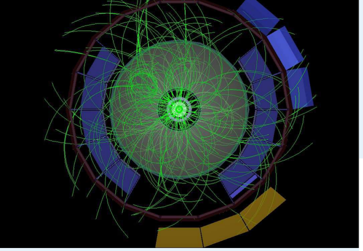

Scales of weakly coupled QGP

- T: energy of hard particles
- gT: thermal masses, Debye screening mass, Landau damping
- g^2T: magnetic confinement, color relaxation, rate for small angle scattering
- g^4T: rate for large angle scattering, $\eta^{-1}T^4$

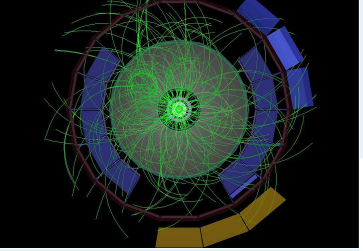

Scales of weakly coupled QGP

- T: energy of hard particles
- gT: thermal masses, Debye screening mass, Landau damping, plasma instabilities [Mrowczynski 1988, 1993, ..]
- g^2T: magnetic confinement, color relaxation, rate for small angle scattering
- g^4T: rate for large angle scattering, $\eta^{-1}T^4$

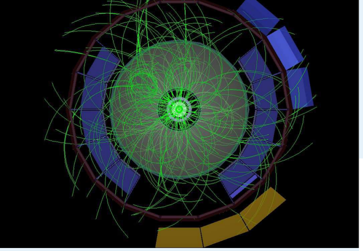

Weibel instabilities

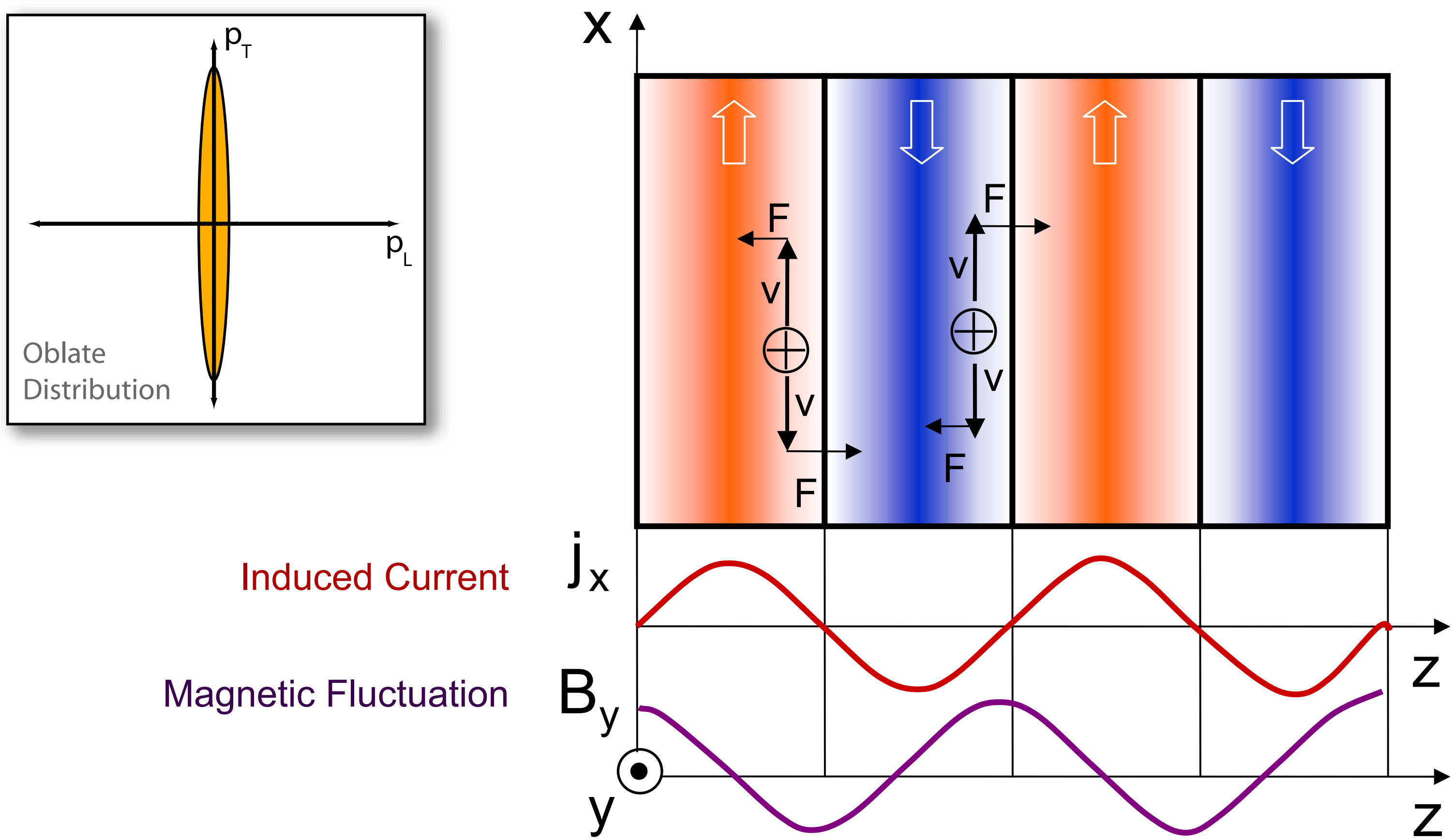

[Strickland 2006]: Illustration of the mechanism of filamentation instabilities.

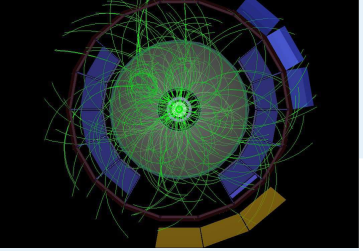

Hard (Thermal) Loops - Boltzmann - Vlasov

Assuming free streaming, one solves the gauge covariant Boltzmann-Vlasov equation

$$v \cdot D\partial f_a(\mathbf{p}, \mathbf{x}, t) = g v_\mu F_a^{\mu\nu} \partial_\nu^{(p)} f_0(\mathbf{p}, \mathbf{x}, t) \tag{1}$$

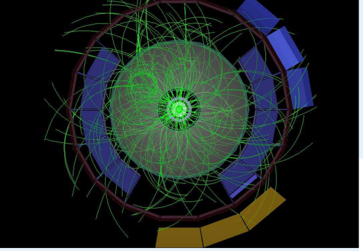

Hard (Thermal) Loops - Boltzmann - Vlasov

Assuming free streaming, one solves the gauge covariant Boltzmann-Vlasov equation

$$v \cdot D\partial f_a(\mathbf{p}, \mathbf{x}, t) = g v_\mu F_a^{\mu\nu} \partial_\nu^{(p)} f_0(\mathbf{p}, \mathbf{x}, t) \qquad (1)$$

coupled to Yang-Mills equation

$$D_\mu F_a^{\mu\nu} = j_a^\nu = g \int \frac{d^3p}{(2\pi)^3} \frac{p^\mu}{2p^0} \delta f_a(\mathbf{p}, \mathbf{x}, t) \qquad (2)$$

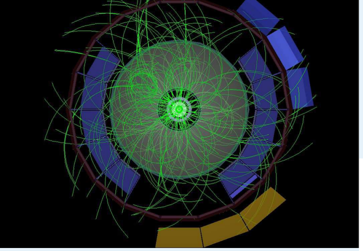

Hard (Thermal) Loops - Boltzmann - Vlasov

Assuming free streaming, one solves the gauge covariant Boltzmann-Vlasov equation

$$v \cdot D\partial f_a(\mathbf{p}, \mathbf{x}, t) = g v_\mu F_a^{\mu\nu} \partial_\nu^{(p)} f_0(\mathbf{p}, \mathbf{x}, t) \tag{1}$$

coupled to Yang-Mills equation

$$D_\mu F_a^{\mu\nu} = j_a^\nu = g \int \frac{d^3p}{(2\pi)^3} \frac{p^\mu}{2p^0} \delta f_a(\mathbf{p}, \mathbf{x}, t) \tag{2}$$

in the HTL approximation

$$g A_\mu \ll |\mathbf{p}_{hard}|\,, \tag{3}$$

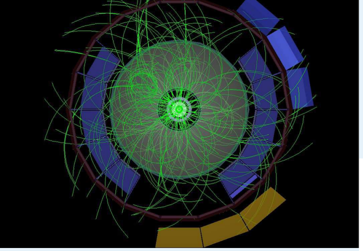

Hard (Thermal) Loops - Boltzmann - Vlasov

Assuming free streaming, one solves the gauge covariant Boltzmann-Vlasov equation

$$v \cdot D\partial f_a(\mathbf{p},\mathbf{x},t) = g v_\mu F_a^{\mu\nu} \partial_\nu^{(p)} f_0(\mathbf{p},\mathbf{x},t) \tag{1}$$

coupled to Yang-Mills equation

$$D_\mu F_a^{\mu\nu} = j_a^\nu = g \int \frac{d^3p}{(2\pi)^3} \frac{p^\mu}{2p^0} \delta f_a(\mathbf{p},\mathbf{x},t) \tag{2}$$

in the HTL approximation

$$g A_\mu \ll |\mathbf{p}_{hard}| \,, \tag{3}$$

the Romatschke, Strickland background distribution function

$$f_0(p_\perp, \tilde{p}_\eta) = f_{\mathrm{CGC}}\left([\mathbf{p^2} + \xi(\tau)(\mathbf{p}\cdot\hat{\mathbf{n}})^2] / p^2_{\mathrm{hard}}(\tau) \right)^{0.5} . \tag{4}$$

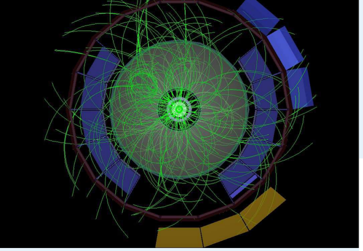

Bjorken expansion

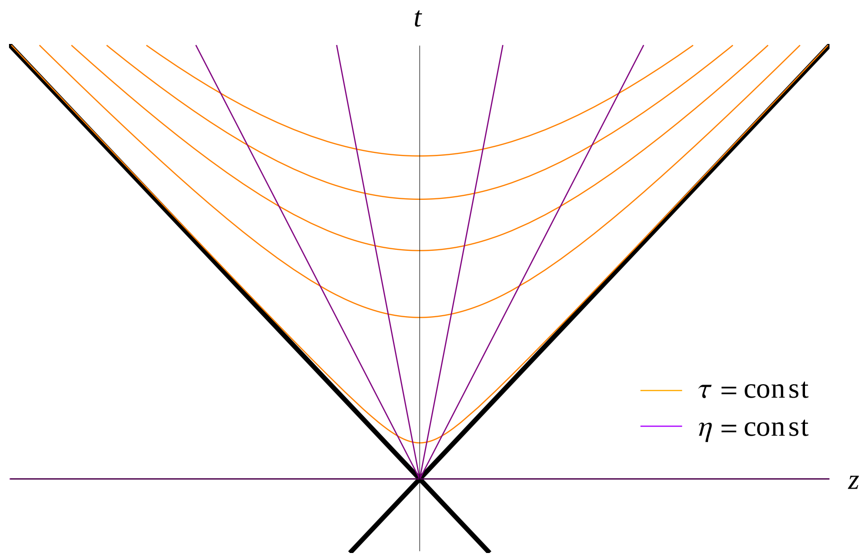

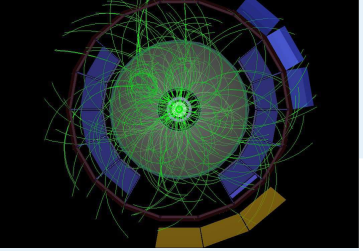

Bjorken expansion

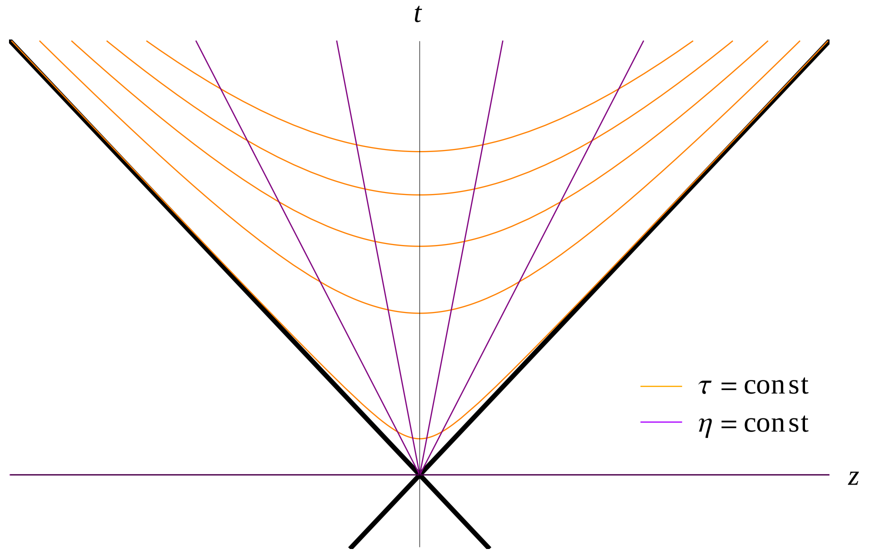

It is convenient to switch to comoving coordinates

$$t = \tau \cosh \eta \,, \qquad \tau = \sqrt{t^2 - z^2} \,,$$
$$z = \tau \sinh \eta \,, \qquad \eta = \operatorname{arctanh} \frac{z}{t} \,, \tag{5}$$

with the corresponding metric

$$ds^2 = d\tau^2 - d\mathbf{x}_\perp^2 - \tau^2 d\eta^2 \,. \tag{6}$$

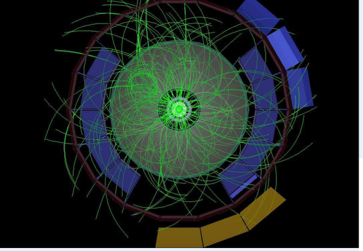

Equation of motions

Yang-Mills equations

$$\tau^{-1}\partial_\tau \Pi_i = j^i - D_j F^{ji} - D_\eta F^{\eta i}\,, \tag{7}$$

$$\tau \partial_\tau \Pi^\eta = j_\eta - D_i F^{i}{}_{\eta}\,. \tag{8}$$

Canonical conjugate field momenta

$$\Pi^i \equiv \tau \partial_\tau A_i, \quad \Pi^\eta \equiv \frac{1}{\tau}\partial_\tau A_\eta\,. \tag{9}$$

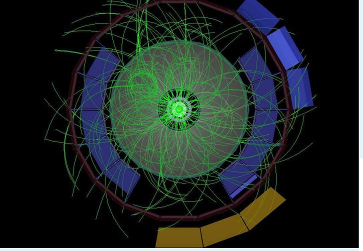

Equation of motions

Yang-Mills equations

$$\tau^{-1}\partial_\tau \Pi_i = j^i - D_j F^{ji} - D_\eta F^{\eta i}\,, \qquad (7)$$

$$\tau\partial_\tau \Pi^\eta = j_\eta - D_i F^{i}{}_{\eta}\,. \qquad (8)$$

Canonical conjugate field momenta

$$\Pi^i \equiv \tau\partial_\tau A_i, \quad \Pi^\eta \equiv \frac{1}{\tau}\partial_\tau A_\eta\,. \qquad (9)$$

The expression for the currents is

$$j^\alpha(\tau,\mathbf{x}_\perp,\eta) = -\frac{m_D^2}{2}\int_0^{2\pi}\frac{d\phi}{2\pi}\int_{-\infty}^{\infty} d\bar{y}\; V^\alpha\,\overline{\mathcal{W}}(\tau,\mathbf{x}_\perp,\eta;\phi,\bar{y})\,,$$

$$m_D^2 = -g^2 t_R\int_0^\infty \frac{dp\,p^2}{(2\pi)^2} f'_{\rm iso}(p)\,. \qquad (10)$$

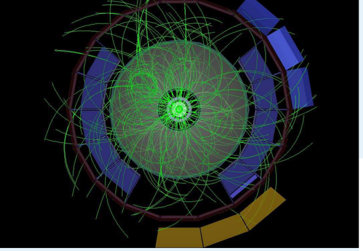

Equation of motions II

The auxiliary fields satisfy

$$\partial_\tau \overline{\mathcal{W}}(\tau, \mathbf{x}_\perp, \eta; \phi, \bar{y}) = -\frac{1}{\cosh \bar{y}} \left[v^i D_i \overline{\mathcal{W}} + \frac{\sinh \bar{y}}{\tau} \left(D_\eta \overline{\mathcal{W}} - \partial_{\bar{y}} \overline{\mathcal{W}} \right) \right] + \frac{1}{\bar{f}(\tau, \tau_{\text{iso}}, \bar{y})} \left[\frac{1}{\tau} v^i \Pi_i - \frac{\tau^2 \sinh \bar{y}}{\tau_{\text{iso}}^2} \Pi^\eta + \frac{\tanh \bar{y}}{\tau} \left(1 - \frac{\tau^2}{\tau_{\text{iso}}^2} \right) v^i F_{i\eta} \right], \tag{11}$$

by replacing y with $\bar{y} \equiv y - \eta$ and

$$\bar{f}(\tau, \tau_{\text{iso}}, \bar{y}) = \left(1 + \frac{\tau^2}{\tau_{\text{iso}}^2} \sinh^2 \bar{y} \right)^2 . \tag{12}$$

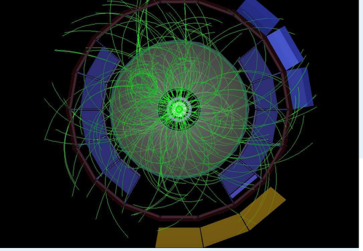

Equation of motions III

We can translate the continuum equations of motion into gauge-invariant lattice equations of motion by using standard plaquette and staple operators

$$(F_{k\eta})^a = \frac{iN_c}{a_\eta}\,\mathrm{tr}\left[\tau^a U_{\Box,k\eta}\right] \tag{13}$$

with the standard plaquette $U_{\Box,\mu\nu}(x) = U_\mu(x)U_\nu(x+\mu)U^\dagger_\mu(x+\nu)U^\dagger_\nu(x)$.
Express the covariant derivatives of the field strength tensor

$$(D_\eta F_{\eta j})^a = \frac{iN_c}{a_\eta^2}\,\mathrm{tr}\left[\tau^a U_j(\tau,x)\sum_{|\eta|\neq j} S^\dagger_{j\eta}(\tau,x)\right] \tag{14}$$

with the gauge link staple

$$S^\dagger_{\mu\nu}(\tau,x) = U_\nu(\tau,x+\mu)U^\dagger_\mu(\tau,x+\nu)U^\dagger_\nu(\tau,x)\,. \tag{15}$$

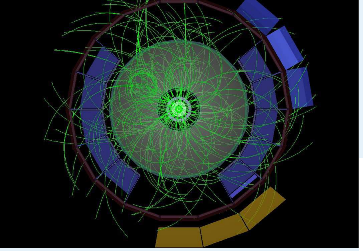

Lattice parameters

The η lattice spacing is determined by

$$\nu_{\text{min}} = \frac{2\pi}{N_\eta a_\eta} \ll 5\,. \tag{16}$$

The infrared cutoff in the transverse direction fullfills

$$k_{\text{min}} = \frac{2\pi}{N_\perp a} \ll 0.2\,\tau_0^{-1}\,. \tag{17}$$

The time dependent longitudinal UV cutoff

$$\nu_{\text{max}} = \frac{\pi}{a_\eta \tau} \gg 30 \tag{18}$$

and the constant transverse UV cutoff should be comparable

$$k_{\text{max}} = \frac{\pi}{a} \gg Q_s\,. \tag{19}$$

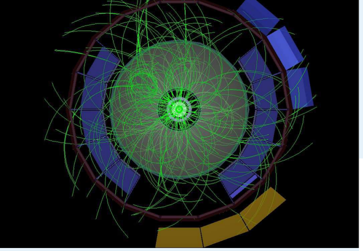

Unstable modes growth rate

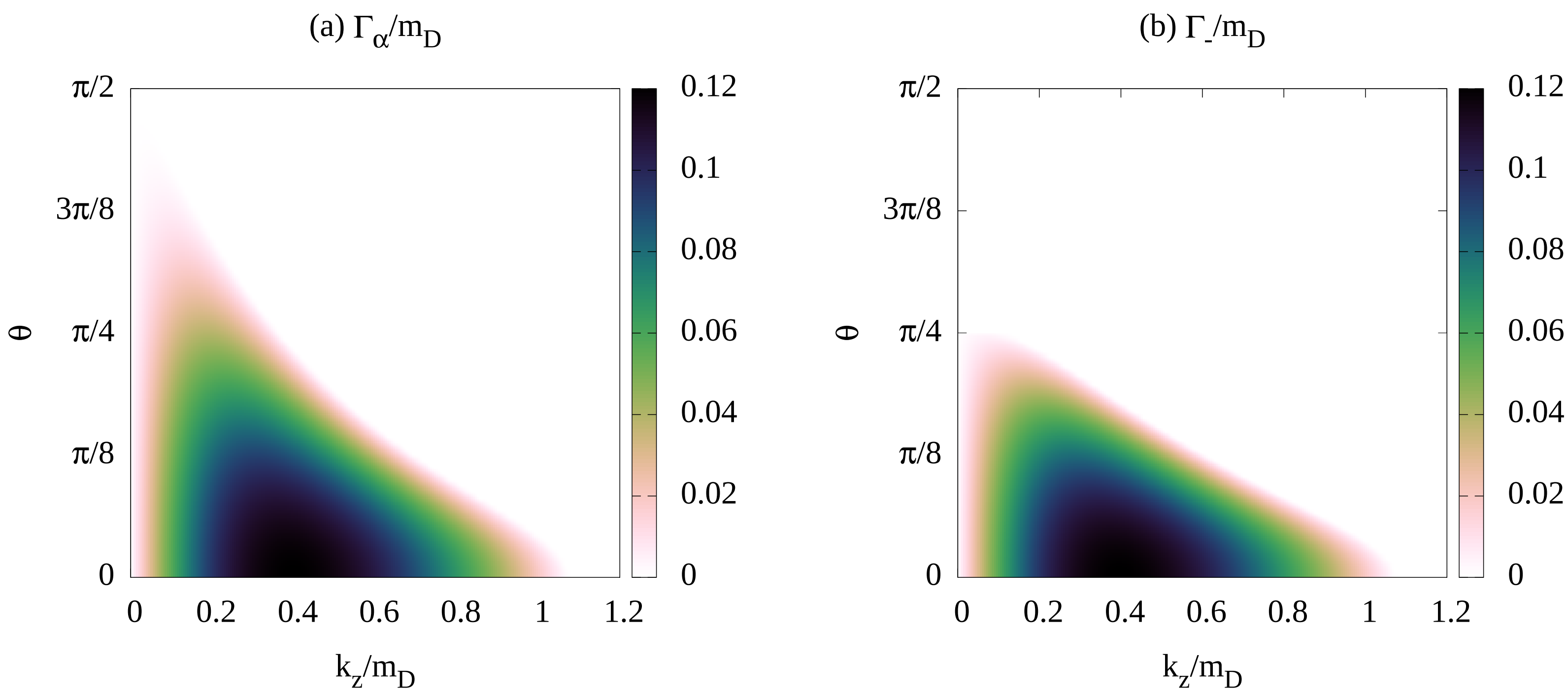

General k growth rates for the α and $-$ modes for $\xi = 10$ with general k as $\theta = arctan(k_\perp / k_\eta)$

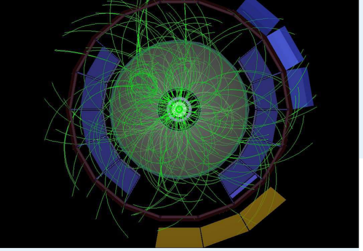

Unstable modes growth rate

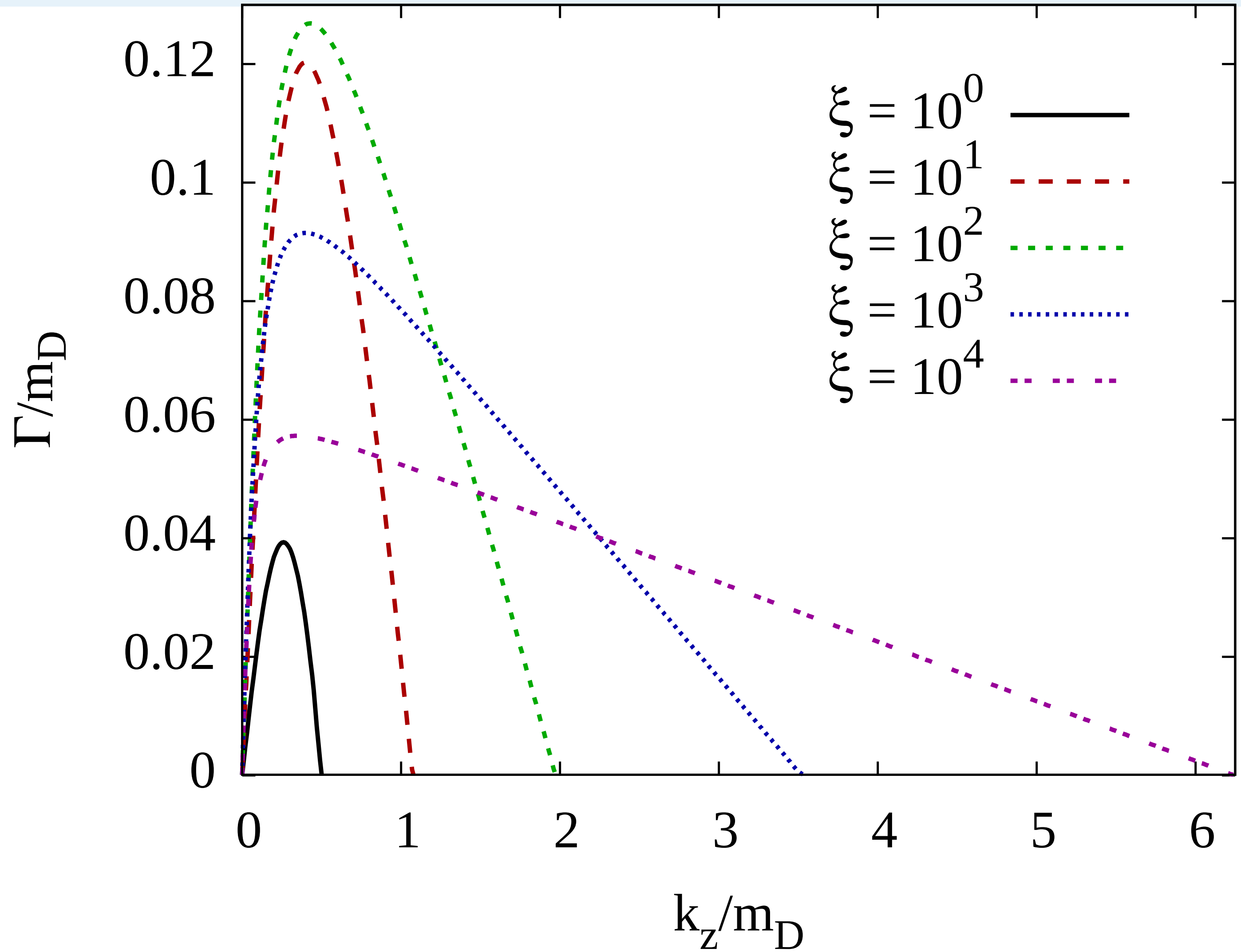

Unstable mode spectra of purely longitudinal modes for specific anisotropies: $N(\tau) \approx \exp(2m_D\sqrt{\tau\tau_{\mathrm{CGC}}})$

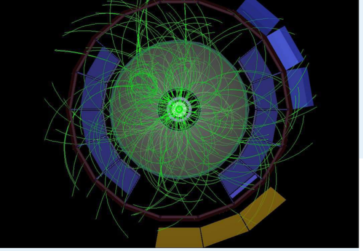

Anisotropy occupancy

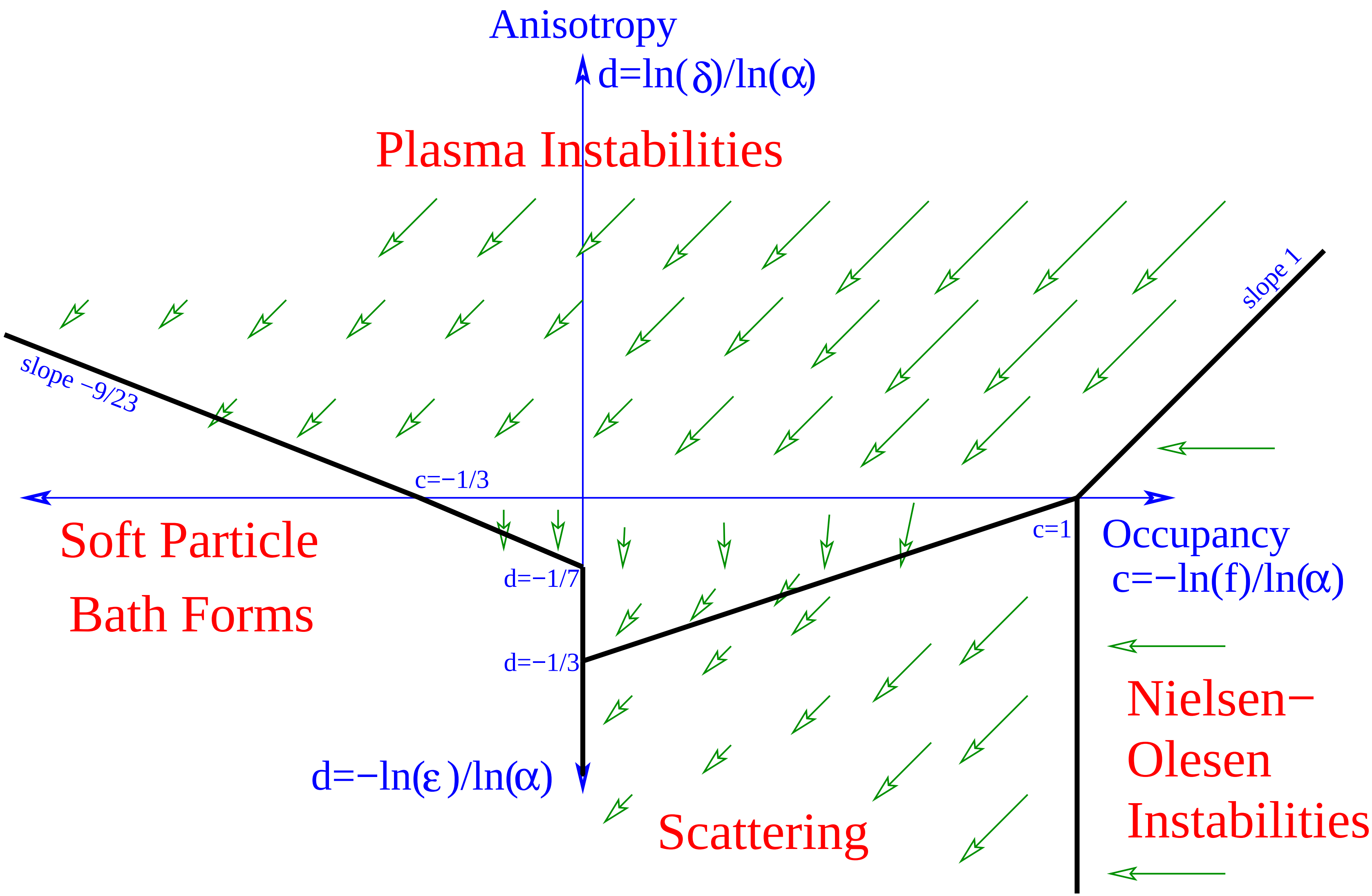

[Kurkela, Moore 2012]: Thermalization in Weakly Coupled Nonabelian Plasmas.

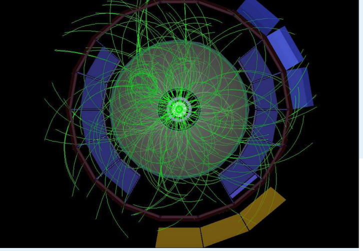

Expanding 3D+3V non-Abelian Plasma Instabilities

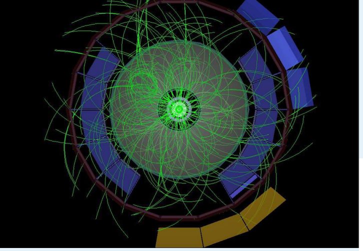

HEL checks

3D+3V fixed box limit

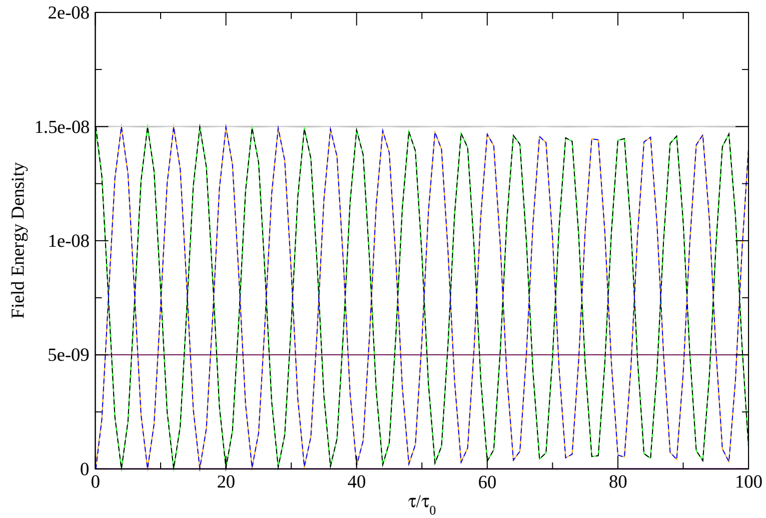

1D+3V semi-analytical results

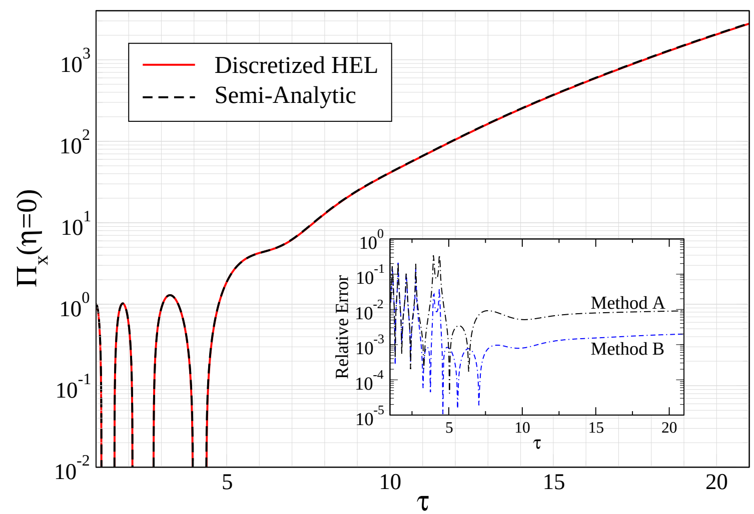

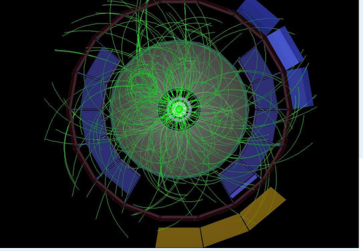

HEL checks II

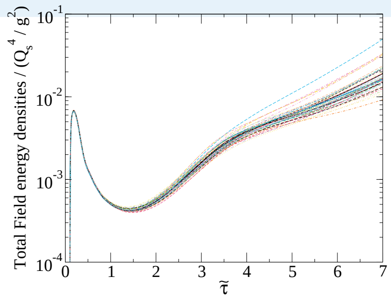

(a) Different seeds

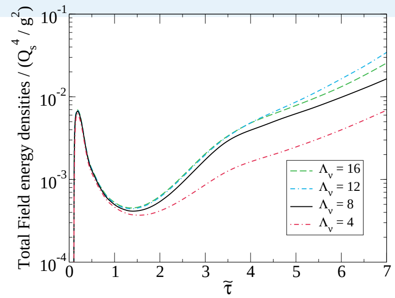

(b) Variation of Λ_ν

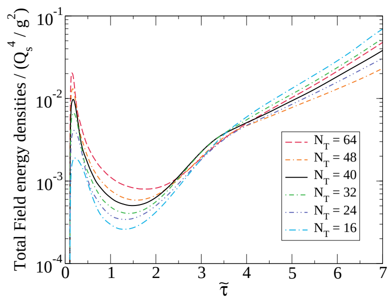

(c) Variation of $a_\perp$

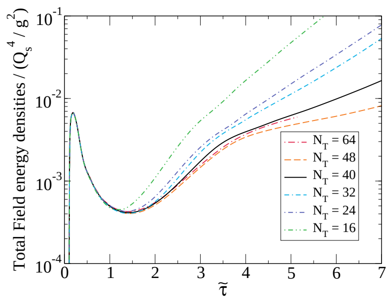

(d) Variation of $N_\perp$

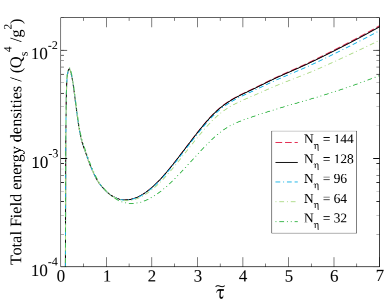

(e) Variation of a_η

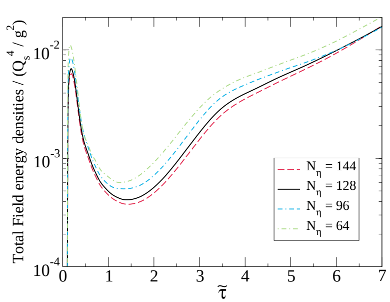

(f) Variation of N_η

Figure 1: Numerical check

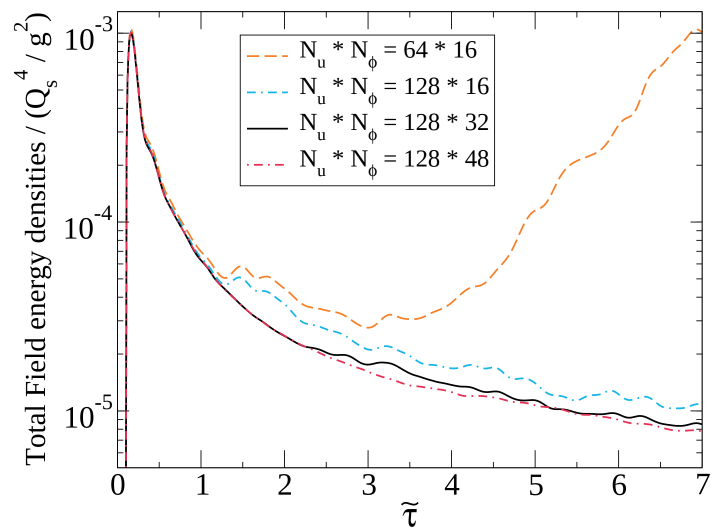

Figure 2: Evolution of stable modes

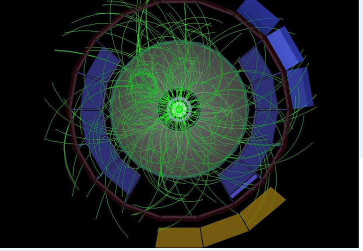

Energy densities fields

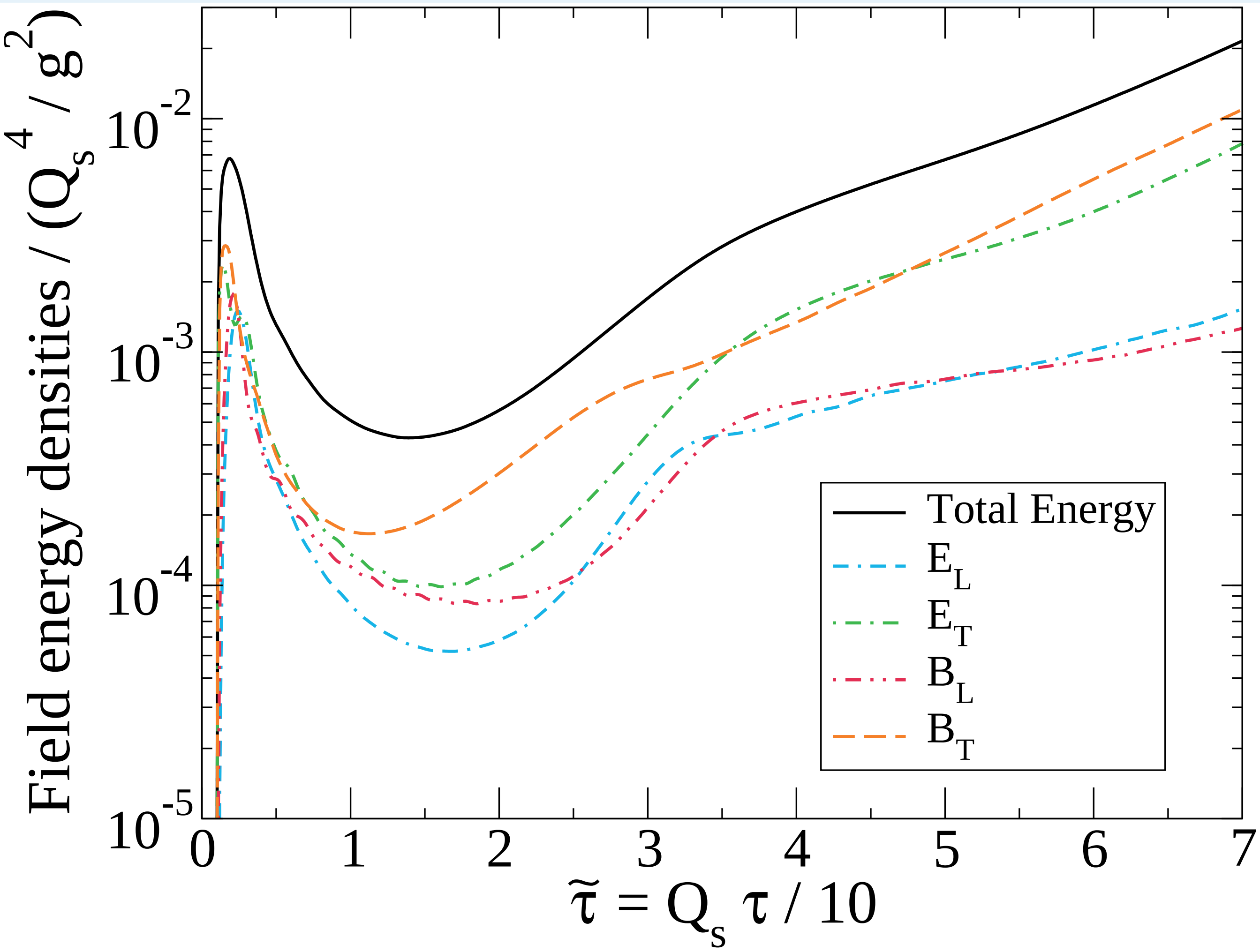

Figure 3: 50 averaged runs $N_\perp * N_\eta * N_u * N_\phi = 40^2 * 128 * 128 * 32$: after onset one sees **rapid growth of B_l and E_L fields**, followed by non-Abelian interactions kick in.

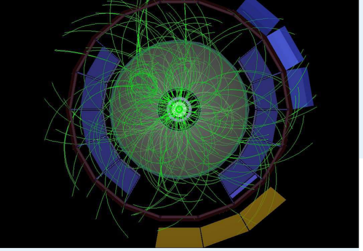

Energy densities fields

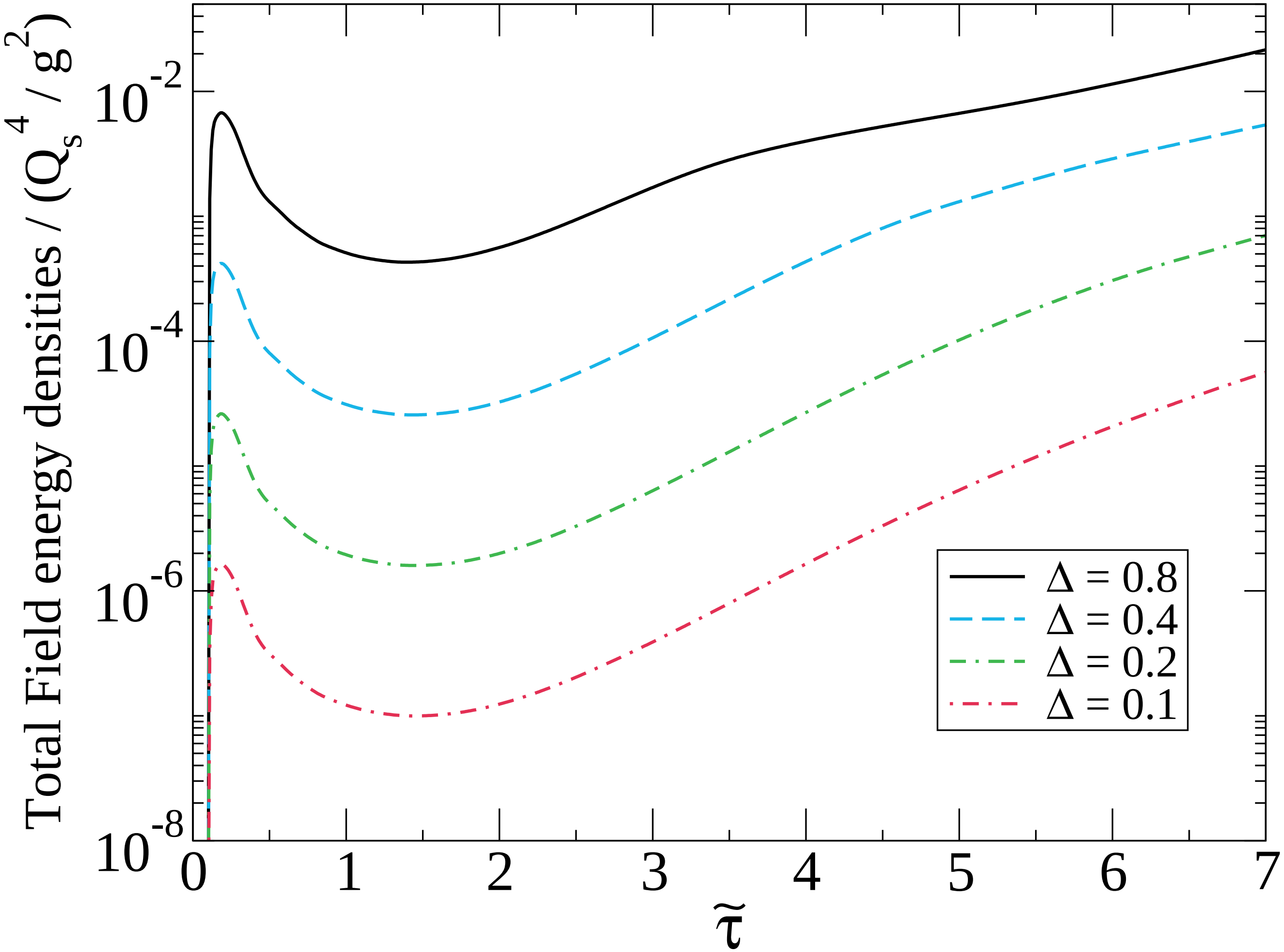

Figure 4: Total field energy density for different initial current fluctuation magnitudes showing similar behavior (apart from non-Abelian point).

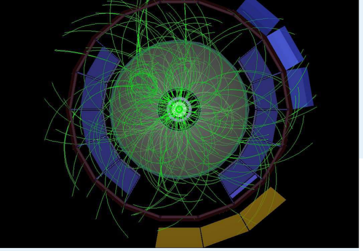

Pressures

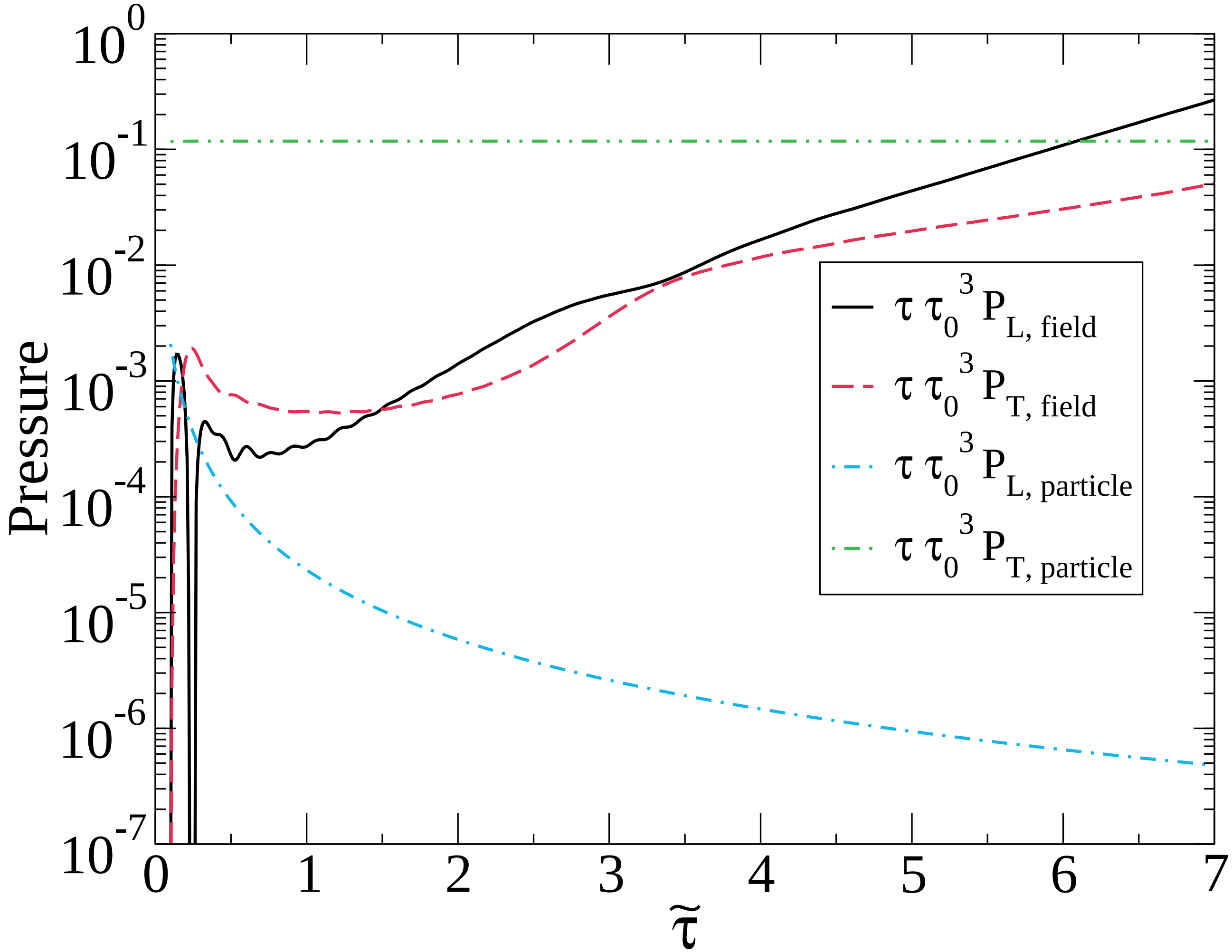

Figure 5: Initially highly anisotropic, note $P_{L,\mathrm{field}}(\tau = 0.3) < 0$, **growing field pressures**, $P_{L,\mathrm{field}}$ dominates at late times, $\tilde{\tau}$ scaled P_L drops $\propto 1/\tilde{\tau}^2$.

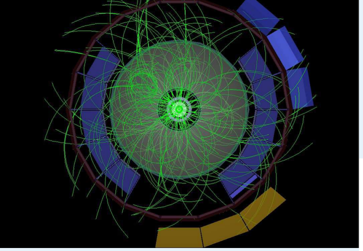

Pressure ratio

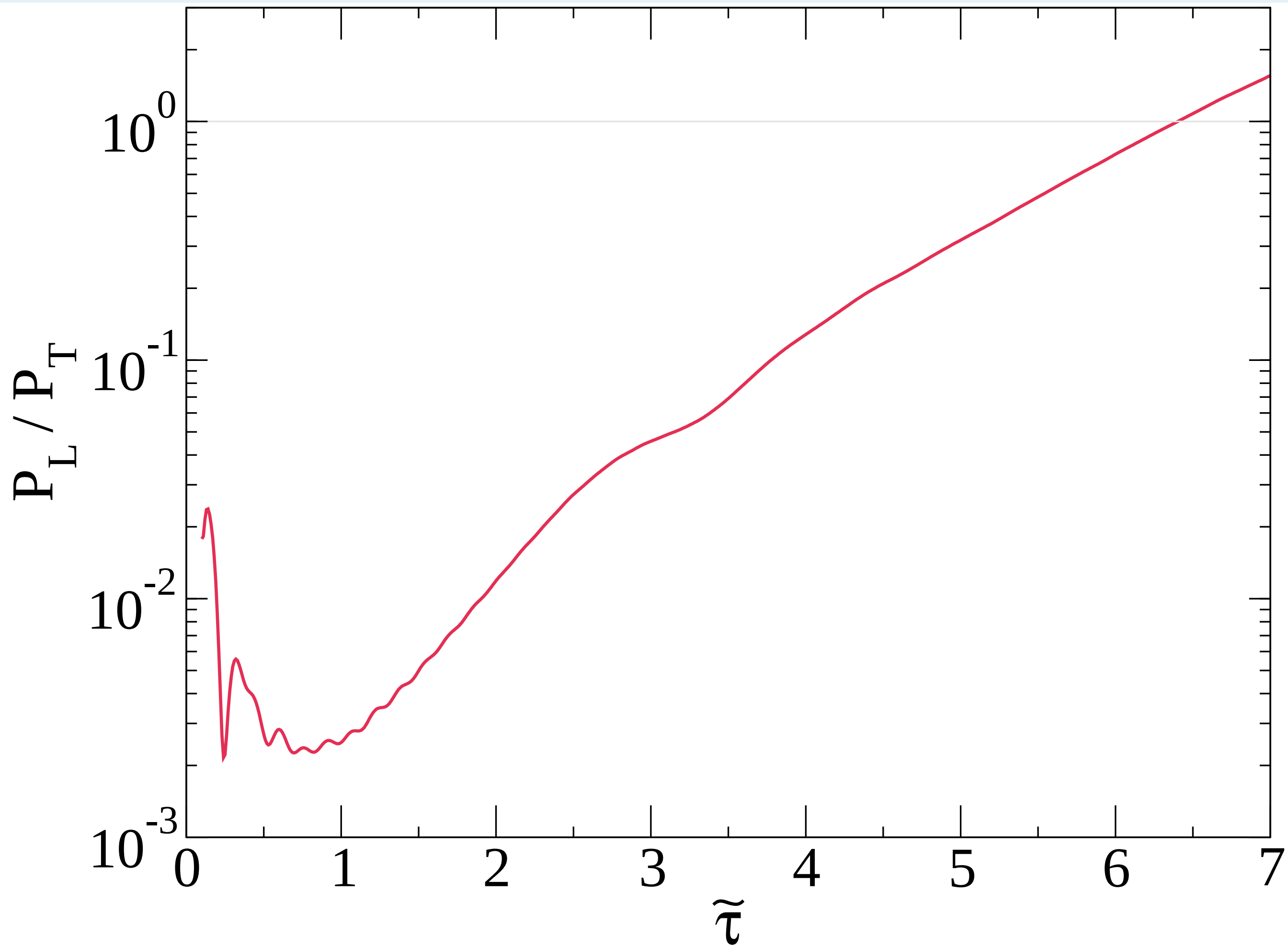

Figure 6: Chromo-Weibel instability **restores isotropy** on fm/c scale, at $\tilde{\tau} \approx 6$.

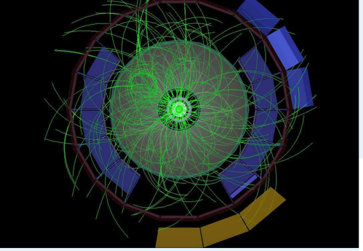

Pressure ratio

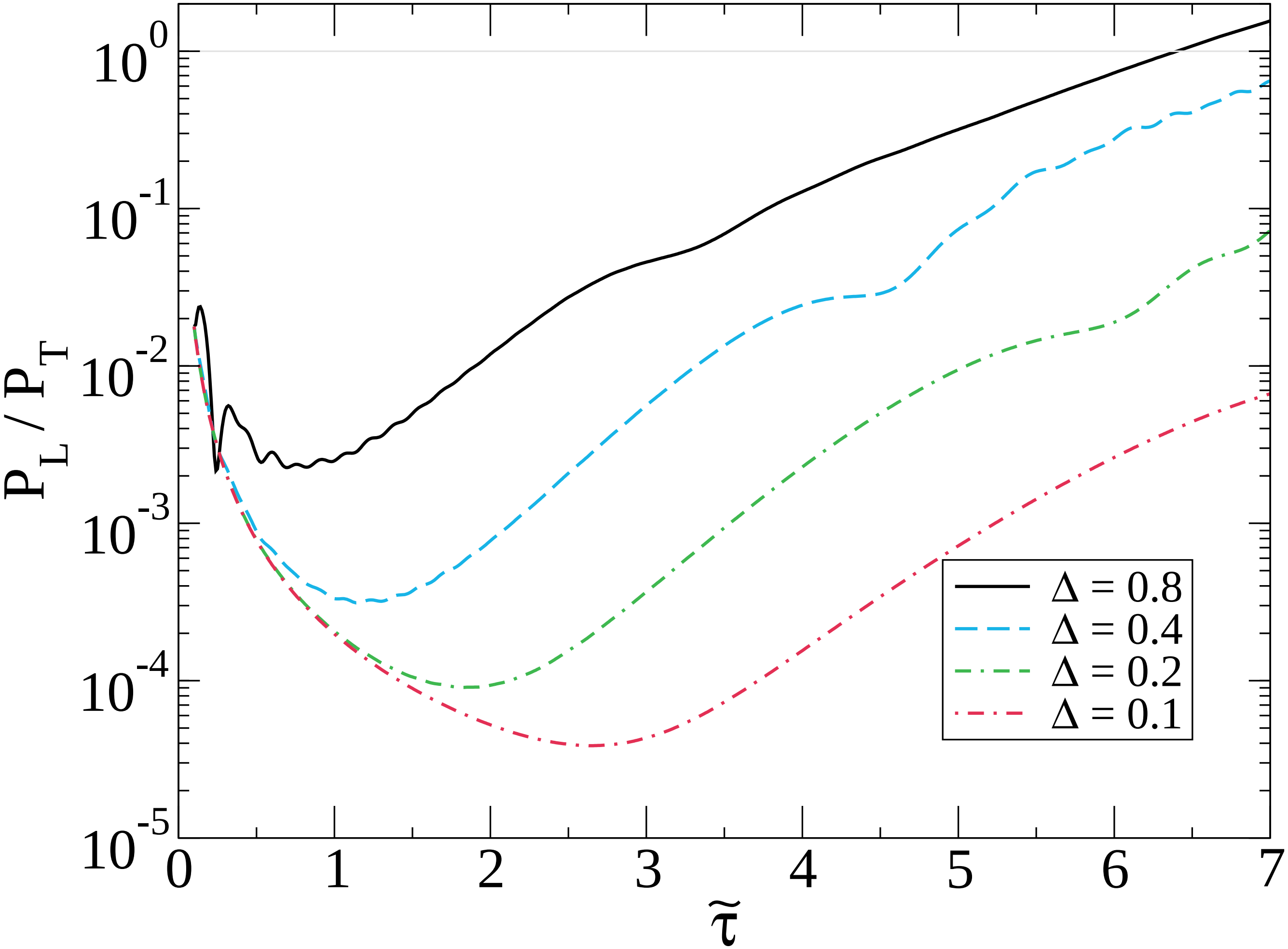

Figure 7: Different initial current fluctuation magnitudes Δ effecting the isotropization time.

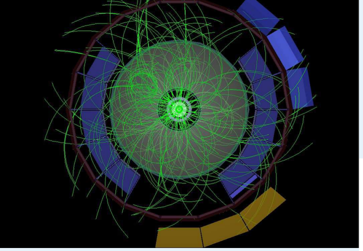

Non-Abelian spectra

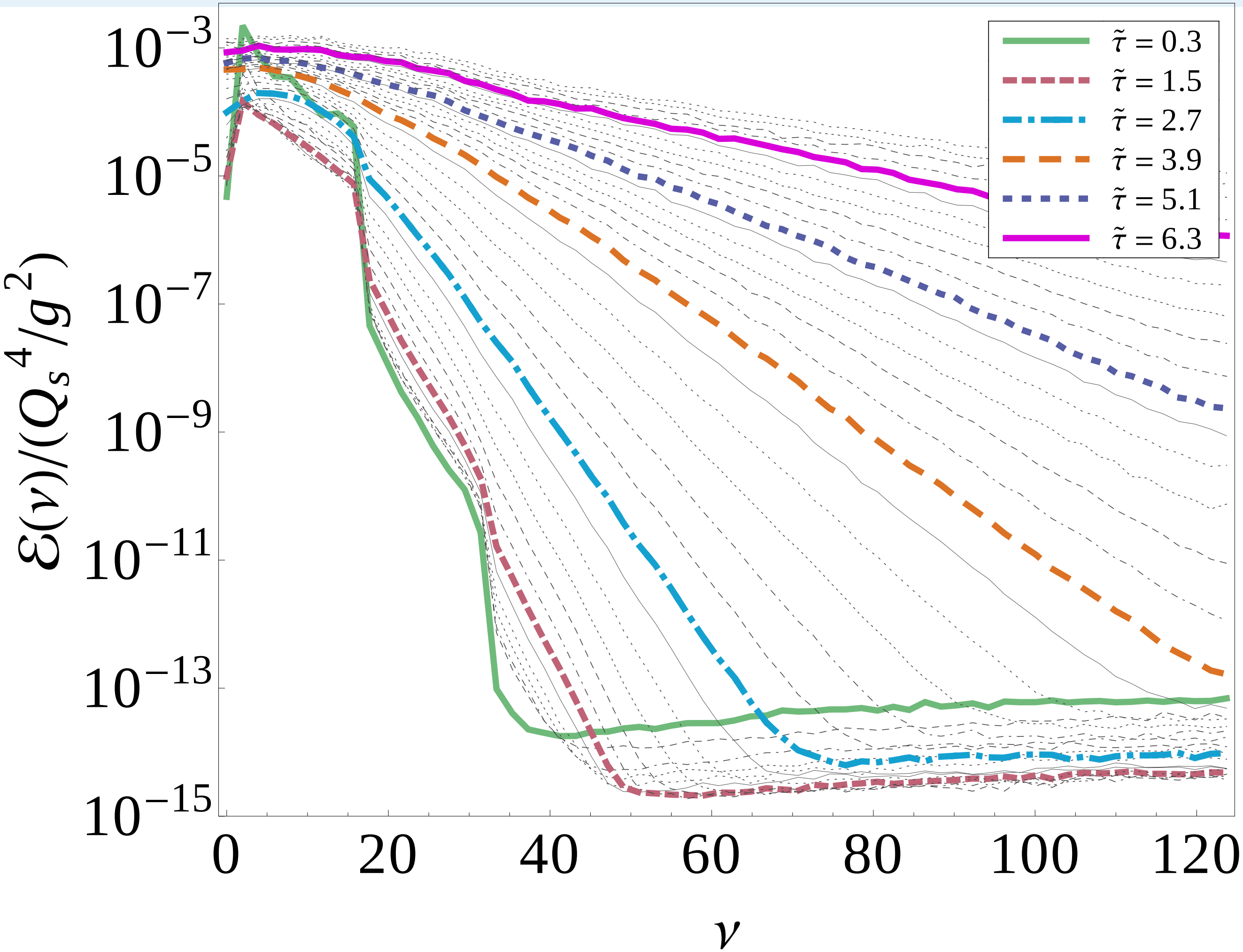

Figure 8: Fourier transform each E and B chromofields and sum all the components: **rapid emergence of an exponential distribution of longitudinal energy**.

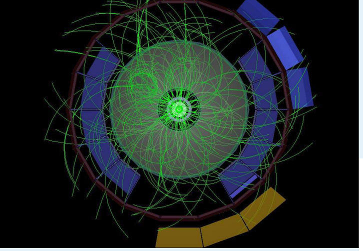

Abelian spectra

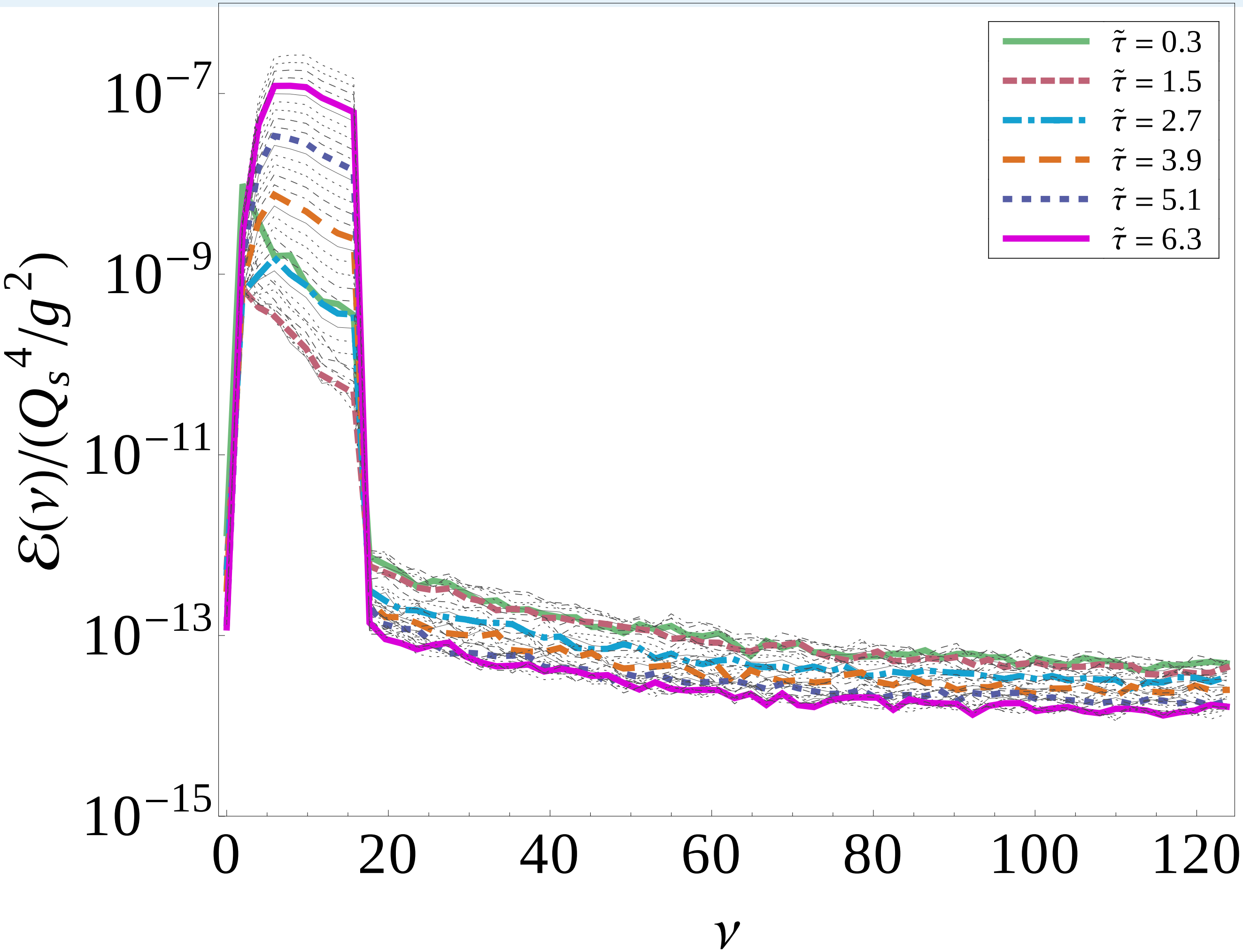

Figure 9: Longitudinal spectra for **abelian** runs shows amplification of the initial seeded modes.

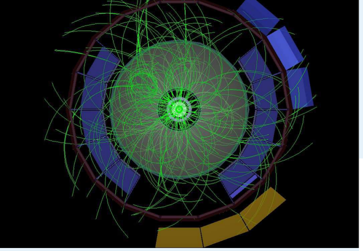

Spectra

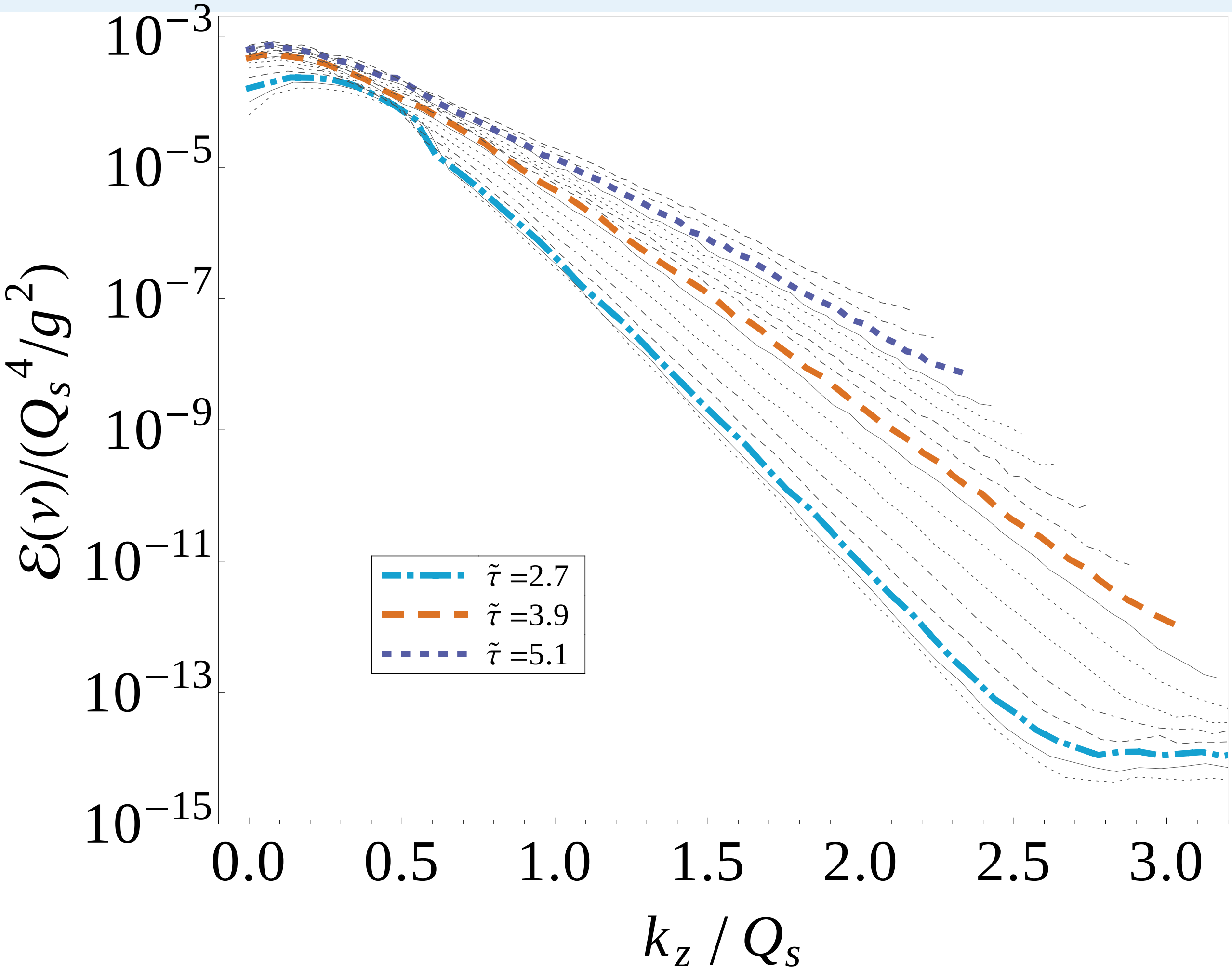

Figure 10: The **red-shifting** is even more visible in the k_z plot. Nonlinear mode-mode coupling is vital in order to populate high momentum modes.

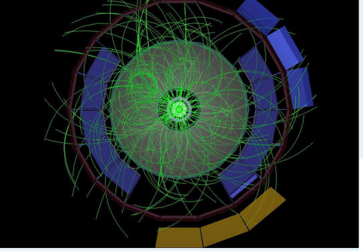

Spectra fits

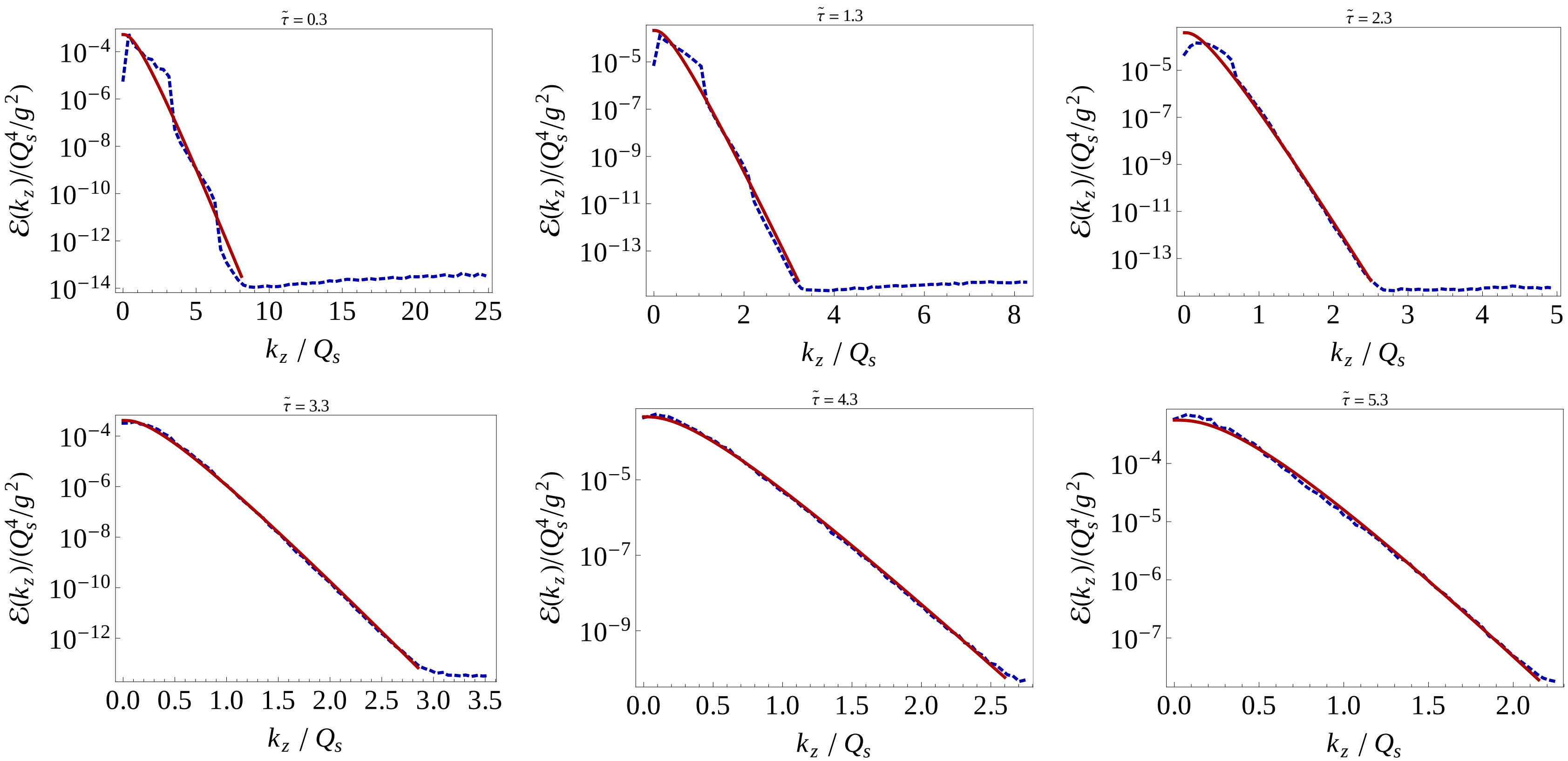

Massless Boltzmann distribution fits the longitudinal spectra:

$$\mathcal{E}_{\rm fit}(k_z) = A\left(k_z^2 + 2|k_z|T + 2T^2\right)\exp\left(-|k_z|/T\right) \qquad (20)$$

Comparison of data and fit function at six different $\tilde{\tau}$.

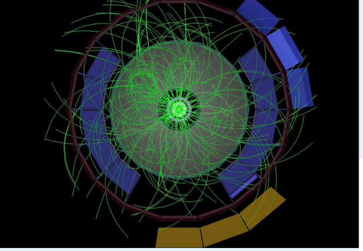

Longitudinal thermalization

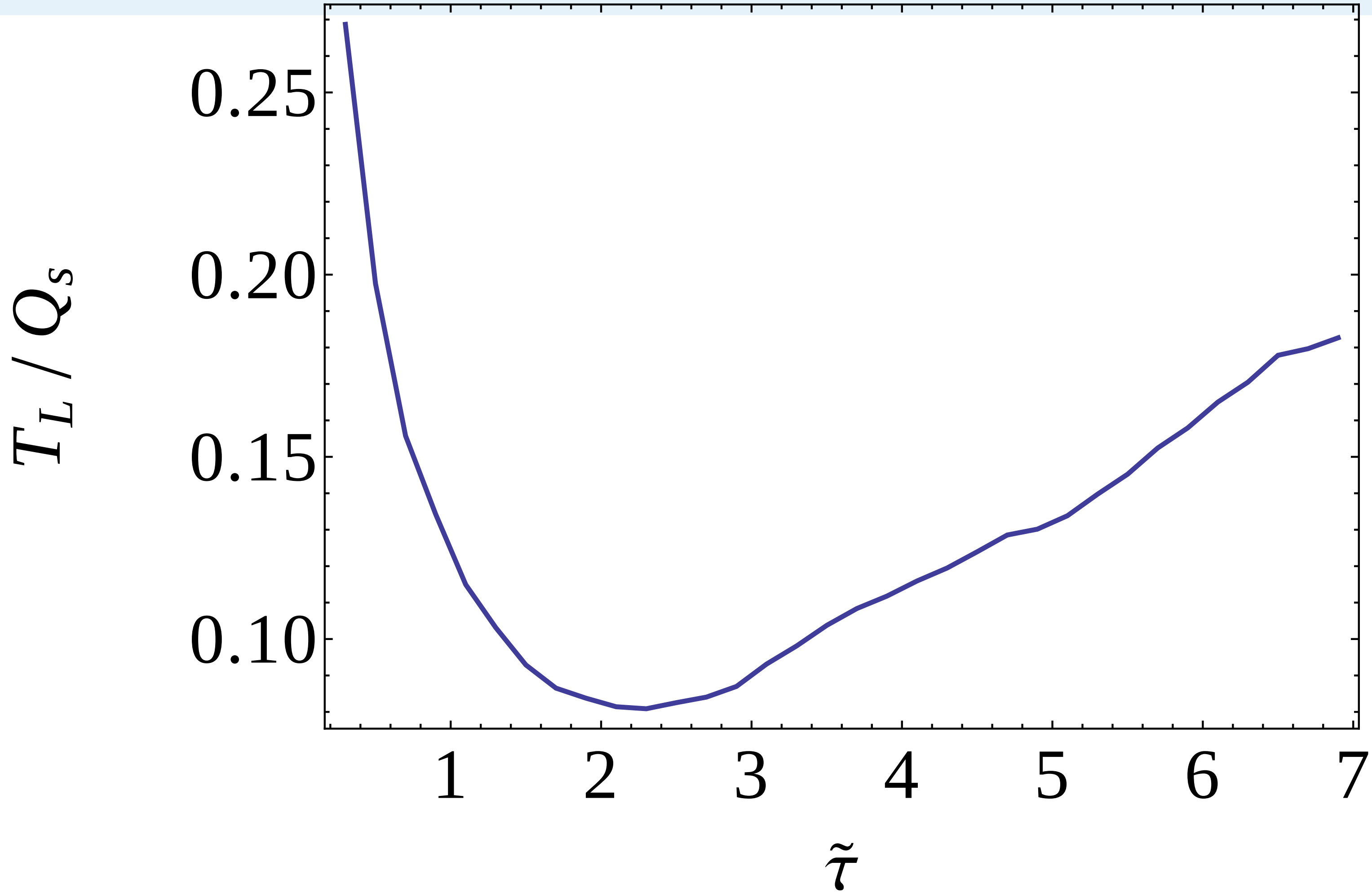

Figure 11: First the soft sector cools down. Due to the instability longitudinal soft **fields reheats**.

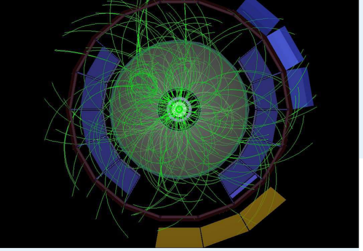

Outlook

- Experimental signatures
- Larger longitudinal N_η (longitudinal parallellization)
- Improved IC conditions: $k_\perp$ cutoff
- Spectral analysis $f_A(k), f_E(k)$
- Probe diagramm with modified f_0
- Incorporate backreaction

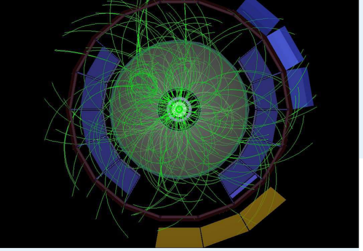

Conclusions

- We performed the **first real-time 3d numerical** study of non-Abelian plasma in a longitudinally expanding system within hard expanding loops HEL.
- The **momentum space anisotropy** can persist for quite some time.
- There doesn't seem to be a "soft scale" saturation of the instability as was seen in static boxes.
- The longitudinal spectra seem to be well described by a Boltzmann distribution indicating **rapid longitudinal thermalization of the gauge fields**.
- We are now studying even larger lattices in order to better understand the infrared dynamics.

Real-time lattice parameters of the hamiltonian evolution in temporal axial gauge:

longitudinal lattice spacing	a_η	0.025
transverse lattice spacing	a	Q_s^{-1}
temporal time step	ϵ	$10^{-2}\tau_0$
first time step	τ_0	$1/Q_s$
longitudinal lattice points	N_η	128
transverse lattice points	$N_\perp$	40
lattice size in velocity space	$N_u \times N_\phi$	128×32
coupling constant	g	$(3.77)^{0.5}$

Assuming for LHC collisions

$$Q_s \sim 2\mathrm{GeV} = (0.1\mathrm{fm})^{-1}\ . \tag{21}$$

We match to CGC values

$$n(\tau_0) = c\frac{N_g Q_s^3}{4\pi^2 N_c \alpha_s (Q_s\tau_0)} \tag{22}$$

with the gluon liberation factor $c = 2\ln 2$. From this one can determine the CGC Debye mass

$$m_D^2(\tau_{\mathrm{CGC}}) = 1.285/(\tau_0\tau_{\mathrm{CGC}}). \tag{23}$$